Editors' Suggestion

Imaging of Submicroampere Currents in Bilayer Graphene Using a Scanning Diamond Magnetometer

M.L. Palm,[1,§] W.S. Huxter,[1,§] P. Welter,[1] S. Ernst,[1] P.J. Scheidegger,[1] S. Diesch,[1] K. Chang,[1,†] P. Rickhaus,[1,‡] T. Taniguchi,[2] K. Watanabe,[3] K. Ensslin,[1,4] and C.L. Degen[1,4,*]

[1] *Department of Physics, ETH Zurich, Otto Stern Weg 1, Zurich 8093, Switzerland*

[2] *International Center for Materials Nanoarchitectonics, National Institute for Materials Science, 1-1 Namiki, Tsukuba 305-0044, Japan*

[3] *Research Center for Functional Materials, National Institute for Materials Science, 1-1 Namiki, Tsukuba 305-0044, Japan*

[4] *Quantum Center, ETH Zurich, Zurich 8093, Switzerland*

(Received 25 January 2022; accepted 28 March 2022; published 5 May 2022)

We report on nanometer magnetic imaging of two-dimensional current flow in bilayer graphene devices at room temperature. By combining dynamical modulation of the source-drain current with ac quantum sensing of a nitrogen-vacancy center in the diamond probe tip, we acquire magnetic field and current density maps with excellent sensitivities of 4.6 nT and 20 nA/μm, respectively. The spatial resolution is 50–100 nm. We introduce a set of methods for increasing the technique's dynamic range and for mitigating undesired back-action of magnetometry operation (scanning tip, laser and microwave pulses) on the electronic transport. Finally, we show that our imaging technique is able to resolve small variations in the current flow pattern in response to changes in the background potential. Our experiments demonstrate the feasibility for detecting and imaging subtle spatial features of nanoscale transport in two-dimensional materials and conductors.

DOI: 10.1103/PhysRevApplied.17.054008

I. INTRODUCTION

Electronic transport in nanostructures and thin films shows a rich variety of physical effects that have been fundamental to the development of modern electronics and communication devices. The standard method for investigating electronic transport (resistance measurements) does not provide detailed information on the nanoscale current distribution in such structures. The lack of spatial information is unfortunate, because the current distribution plays a key role in many intriguing physical phenomena. Having a technique that could simply look at nanoscale current flow would be immensely valuable.

In the recent past, researchers have made significant progress in the submicrometer imaging of nanoscale transport phenomena using scanning probe techniques [1]. For example, scanning gate microscopy has been applied to image branched flow [2], universal conductance fluctuations [3], beam collimation [4] and viscous electron flow [5]. Scanning superconducting quantum interference device-on-tip microscopy has been used for the thermal imaging of dissipation [6], the magnetic imaging of persistent edge currents [7], and twist-angle disorder [8] in graphene devices. Scanning single-electron transistors have demonstrated simultaneous mapping of electrostatic potential and current to visualize ballistic and hydrodynamic electron flow [9,10]. Scanning diamond magnetometers based on nitrogen-vacancy (N-V) centers have been used to record current profiles in ohmic and hydrodynamic transport regimes in graphene [11–13] and semimetals [14]. Overall, these techniques have opened an exciting avenue for imaging nanoscale transport phenomena in real space.

Recent demonstrations with scanning diamond magnetometers applied fairly large source-drain currents, of the order of a few microamperes [12,14,15] to a few tens of microamperes [11–15], because of sensitivity limitations. Although some phenomena can be observed under these conditions, high current densities are in general undesirable, as they can cause, for example, a heating of the electron gas [16] or nonlinearities due to large source-drain potentials [17]. Moreover, spatial features of interest often only amount to changes of a few percent in the total

*degenc@ethz.ch

†Present address: Aeva Inc., 555 Ellis St., Mountain View, CA 94043, USA.

‡Present address: Qnami AG, Hofackerstrasse 40B, 4132 Muttenz, Switzerland.

§These authors contributed equally.

 © 2022 American Physical Society

current density, leading to challenges in background suppression. Another concern is the influence of the probe tip [3,18], the optical readout [19–21], and the microwave spin manipulation [15] on the transport properties. All of these issues provide strong motivation for further improving the sensitivity of the technique and exploring methods for mitigating undesired stray effects.

In this work, we present advances to the sensitive and noninvasive imaging of current flow in two-dimensional materials using scanning diamond magnetometry. Our samples are bilayer graphene (BLG) devices encapsulated in hexagonal boron nitride (*h*-BN). We demonstrate coherent detection of modulated (kilohertz to megahertz) currents with submicroampere sensitivity and introduce a Bayesian quantum-phase unwrapping method for resolving small current density variations on top of large background currents. We also investigate and mitigate the influence of the scanning tip, laser, and microwave pulses on the transport properties. We analyze current density maps for spatial variations in conductivity and show that the flow pattern can be deliberately changed by adjusting the carrier density via the back-gate potential. Finally, in contrast to recent imaging of monolayer graphene (MLG) [11,12], we observe no signatures of hydrodynamic transport for our BLG devices at room temperature.

II. SETUP AND DEVICES

A schematic of our experiment is shown in Fig. 1(a). We study current flow in patterned graphene devices by recording magnetic field maps above the surface using a diamond scanning probe with an N-*V* center tip [23,24]. Devices are fabricated from a single BLG sheet that is encapsulated between two layers of *h*-BN using mechanical exfoliation and stacking in a dry transfer process [25,26]. The van der Waals stack is located on top of

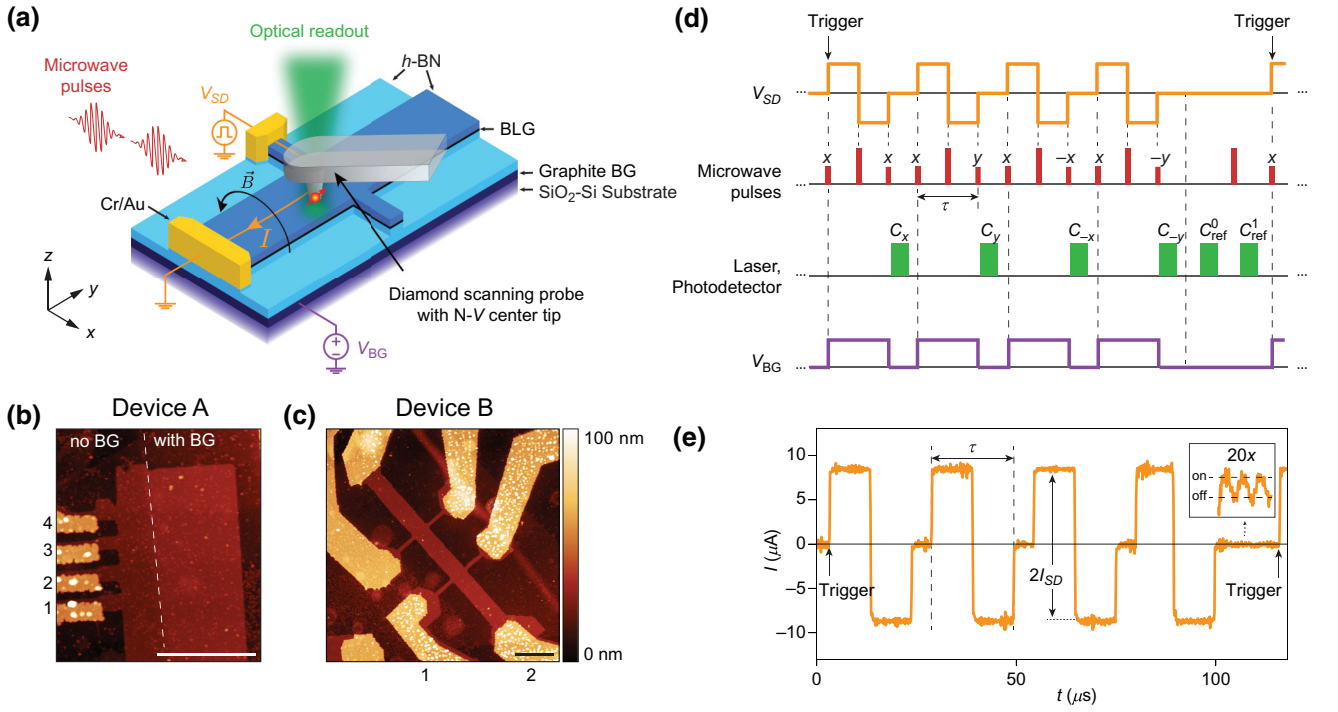

FIG. 1. Schematic of the current imaging experiment. (a) We use a nitrogen-vacancy center (red) in a diamond tip (gray) to image the magnetic stray field appearing above a current-carrying graphene device. Microwave (dark red) and laser pulses (green) are used to manipulate and read out the spin state of the N-*V* center [22]. The device consists of a bilayer graphene (BLG) sheet encapsulated in hexagonal boron nitride (*h*-BN, 11 nm top and 27 nm bottom thickness) that sits on top of a graphite back gate (BG). V_{SD} and V_{BG} are source-drain and back-gate voltages, respectively. (b,c) Atomic force microscopy images of the two devices used in this study. Note that device A is only partially covered by the back gate (white dashed line). Electrical contacts are numbered. Scale bars are 2 μm. (d) Measurement protocol. We modulate the source-drain voltage V_{SD} (orange), microwave power (red), laser power (green) and back-gate voltage V_{BG} (purple) using an arbitrary waveform generator. Tall microwave pulses are π rotations and short pulses are $\pi/2$ rotations. Labels $x, y, -x, -y$ indicate the pulse phase Φ. τ is the phase accumulation time of the dynamical decoupling sequence (here a spin echo). C^0_{ref} and C^1_{ref} are reference photoluminescence intensities of the two spin states. Triggers indicate the start of a measurement cycle. (e) Measured source-drain current during the experimental protocol (d). The inset shows the effect of laser pulses (on, off) when the tip is positioned near one of the injection points at $V_{SD} = 0$ V (10-point moving-average filter applied). $2I_{SD}$ is the peak-to-peak amplitude of the current signal.

a 4-nm-thick graphite flake acting as a back gate. The final stack is annealed, electrically contacted (Cr/Au) [25], and patterned through e-beam lithography and reactive ion etching. Two device geometries are used in this study. Device A is named the "four-terminal device" and is only partially covered by the back gate [Fig. 1(b)]. Device B has a Hall-bar geometry and is fully covered by the back gate [Fig. 1(c)]. Both devices are made from the same van der Waals stack. These device geometries featuring elongated channels and side-injectors are commonly used to study hydrodynamic electron flow [5,12,27]. The partially back-gated device further allows us to study how transport is affected by locally changing the carrier density of the BLG sheet. Conventional transport measurements at ambient conditions on the Hall bar (width 0.8 μm, side contact separation 3 μm) yield Hall mobilities for electrons (holes) of $\mu \approx 3.3 \times 10^4$ cm^2/V s (2.4×10^4 cm^2/V s) and mean free paths of $l_m \approx 0.4$ μm (0.3 μm) at a carrier density of 1×10^{12} cm^{-2} (Fig. S1 in the Supplemental Material [28]). The back-gate voltage is zero unless stated otherwise.

Our custom-built scanning magnetometer consists of a three-axis sample stage that is scanned underneath a diamond probe tip in noncontact mode. The diamond tip contains a single N-V center near the apex. The vertical standoff between the N-V center in the tip and the buried graphene sheet during a magnetometry scan is approximately $z = 100$ nm (71 nm N-V standoff distance [28,29], 11 nm h-BN thickness, and 10–30 nm additional scan distance). A single diamond probe (count rate $C_0 \sim 550$ kC/s, spin contrast $\epsilon \sim 26\%$, QZabre AG [30]) is used for all experiments. Optical excitation (520 nm) and detection (630–800 nm) of the N-V spin state are performed via the same objective located above the probe and sample. Microwave excitation is achieved via a short bond wire loop (approximately 30 μm away) that is not mechanically connected to the sample stage. A small bias field of 5–18 mT is applied to separate the N-V $m_S = \pm 1$ spin levels. All measurements are carried out at room temperature.

III. MEASUREMENT TECHNIQUE

We detect the current-generated magnetic field at each pixel using the concept of the quantum lock-in amplifier [12,14,31,32]. We apply a square-wave voltage ($f =$ 50–100 kHz) between the source and drain contacts and synchronize the waveform with the microwave and laser pulses as well as optical detection. To ensure proper synchronization of all channels, we generate all analog and digital signals on a multi-channel arbitrary waveform generator (AWG, Spectrum DN2.663-04); see Fig. 1(d). Another channel of the AWG is used to dynamically adjust the back-gate voltage during measurements.

The signal of the quantum lock-in is the quantum phase ϕ that the N-V spin acquires during the coherent precession time τ [see Fig. 1(d)]. For our protocol, the quantum phase is given by [28,33]

$$\phi = \gamma_e B_{\mathrm{ac}} \tau, \tag{1}$$

where B_{ac} is the signal amplitude and $\gamma_e = 2\pi \times$ 28 GHz/T the gyromagnetic ratio of the N-V electronic spin. We determine ϕ via photoluminescence intensity measurements,

$$C_\Phi = C_0 \left(1 - \frac{\epsilon}{2} + \frac{\epsilon}{2}\cos(\phi + \Phi)\right), \tag{2}$$

where C_Φ is photons per second, C_0 is the photon count rate of the $m_S = 0$ spin state, and ϵ is the optical contrast. Φ is the relative phase of the final $\pi/2$ pulse. By recording C_Φ for the readout phases $\Phi = 0, \pi/2, \pi, 3\pi/2$ (corresponding to the qubit axes x, y, $-x$, $-y$), we can determine the phase over the full $(-\pi; \pi]$ range using the two-argument arctangent [12,34]:

$$\phi_{\mathrm{wrapped}} = \tan^{-1}\left(\frac{C_{-y} - C_y}{C_x - C_{-x}}\right). \tag{3}$$

This "wrapped phase" ϕ_{wrapped} is equal to ϕ modulo 2π. Therefore, for signals exceeding a maximum field $B_{\max} = \pm\pi/(\gamma_e \tau)$, we expect phase wrapping to occur in the image [35]. In this paper we develop suitable phase unwrapping techniques to recover the original phase ϕ with high dynamic range.

IV. CORRELATIVE MAGNETOMETRY AND TRANSPORT MAPS

We begin our measurements by imaging the magnetic field from the four-terminal device (device A). We apply a voltage of $V_{SD} = 65$ mV between contacts 1 and 3 (2 and 4 are floating), corresponding to a current of $I_{SD} \approx$ 8 μA, and use a spin echo sequence [$N = 1, \tau = 10$ μs; see Fig. 1(d)] to detect the ac modulation. Figure 2(a) shows the wrapped quantum phase ϕ_{wrapped} extracted using the procedure of Eqs. (2) and (3). Simultaneously with the phase measurement, we monitor the total photoluminescence signal (see [28]), device topography [Fig. 2(b)], source-drain current amplitude I_{SD} [Fig. 2(c)], and dc offsets of the source-drain current without (with) laser illumination [Figs. 2(d) and 2(e)]. We further measure the Rabi frequency of the N-V spin as a function of tip position in a separate scan [Fig. 2(f)].

The correlative maps shown in Figs. 2(b)–2(e) allow us to monitor whether the tip, laser or microwave irradiation are affecting the transport properties of the device. Proceeding from left to right, the current amplitude map I_{SD} [Fig. 2(c)] reveals a slight increase in the source-drain current when the tip is positioned near the injection or collection points, likely caused by a "scanning gate" effect due

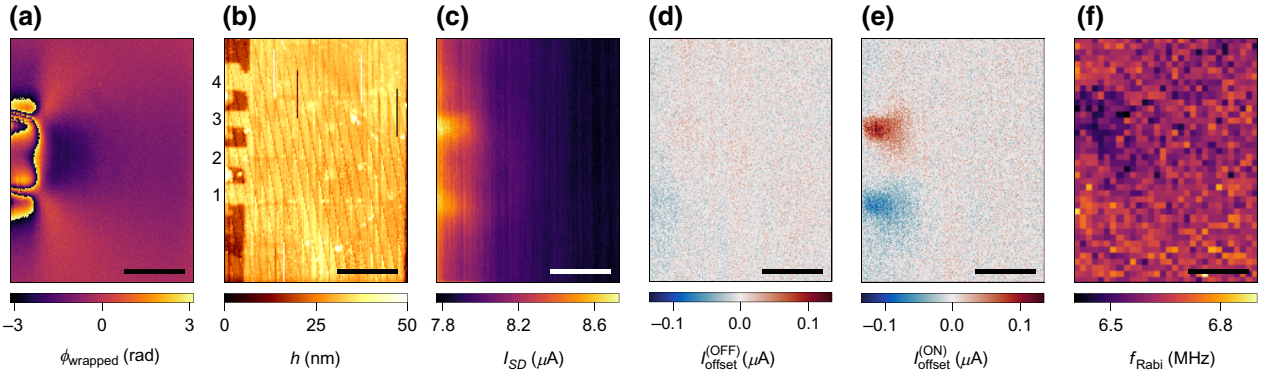

FIG. 2. Correlative maps of magnetometry and transport characteristics. (a) Quantum phase recorded by the scanning magnetometer, according to Eqs. (2)–(3). (b) Topography recorded by the position feedback of the scanning magnetometer. (c) Alternating current amplitude of the source-drain current. (d),(e) Direct current offset of the source-drain current while the laser is (d) off and (e) on (see [28] for more details). Global offsets have been subtracted from both images. (f) Rabi frequency of the N-V spin, recorded separately. Scale bars are 1 μm.

to trapped charges on the diamond tip or photodoping (see below). Other measurements on the same device with the same N-V center at a later stage show no tip influence or a reduction of the source-drain current with the tip positioned near a contact, showing that this effect is small but somewhat random. Next, maps of the dc offset measured with the laser off and on [Figs. 2(d) and 2(e), respectively; see Figs. 1(d) and 1(e) for protocol] show that laser illumination can induce a small photocurrent, especially when the tip is near the metallic contacts. This photocurrent effect is well known [19,36]; however, the effect is small and does not affect magnetometry because the quantum phase measurement always occurs in the laser off state. In addition, to mitigate photodoping of h-BN, which causes drifts in the carrier density [12,21,28], we ramp V_{BG} to zero during laser pulses [Fig. 1(d)]. Figure 2(f) confirms that the Rabi frequency varies less than 5% over the entire scan window, allowing us to rule out significant coupling of microwave pulses to the graphene device [14,15].

V. PHASE UNWRAPPING

We return to the magnetometry map shown in Fig. 2(a). Because of phase wrapping near the injection points where the current density is high, the phase map cannot be directly inverted to reveal the magnetic field B and the associated current density $\mathbf{J}$. Therefore, in Fig. 3, we develop two strategies to recover the magnetic field map even in the presence of large currents.

A first strategy is to use a variable grid and locally refine the pixel sizes in areas of rapidly changing field [11]. Figure 3(a) displays experimental data taken on device B. The phase map is composed of three separate scans (I–III) with pixel sizes of 10–100 nm. The pixel resolutions are chosen such that the true phase differences between pixels are roughly smaller than π. We unwrap each phase map individually using a standard unwrapping algorithm [37,38], convert the maps to units of magnetic field [Eq. (1) with $\tau = 18$ μs], and interpolate them on a common 20×20 nm^2 grid [28]. The resulting field map is shown in Fig. 3(b). In a last step, we compute the current density map [Fig. 3(c)] by inverting Biot and Savart's law using an inverse filtering technique [15,39,40]. This phase-unwrapping method increases the signal range from $B_{\text{max}} = \pm\pi/(\gamma_e\tau) \approx \pm 1$ μT to $B_{\text{max}} \approx 4.6$ μT (-9.1 μT), corresponding to a 6.8$\times$ increase in dynamic range.

Our second approach to resolving the phase wrapping is based on a Bayesian inference and demonstrated in Figs. 3(d)–3(g) on device A. We proceed in two steps. In a first step, we record two images with different interaction times $\tau_1 = 10$ μs and $\tau_2 = 20.5$ μs, displayed in Fig. 3(d). The interaction times are chosen at high points of the spin echo curve where the sensitivity is maximum (Fig. S10 in the Supplemental Material). For the present N-V center embedded in a diamond with a natural abundance of ^{13}C isotopes, the positions of these maxima (revivals) are set by the applied bias field [41]. Ideally, one would select interaction times that do not share common integer multiples. This could more easily be achieved in isotopically pure diamond. The global phase is then recovered either by inverse-variance weighting or by evaluating the joint probability function $P(B)$ [42,43] (see [28] for details). Figure 3(e) shows the resulting field map. Evidently, the first phase-unwrapping step is not complete and fails in areas of high current density. To improve the field estimation, in a second step, we invoke the fact that the magnetic field is spatially smooth, and therefore neighboring pixels are expected to have similar values. According to Bayes' rule, the updated probability function is given by $P(B|B_{\text{est}}) \propto P_G(B - B_{\text{est}})P(B)$, where $P_G(B - B_{\text{est}})$ is a Gaussian centered around the weighted average of the neighboring pixels [28]. The multiplication introduces an

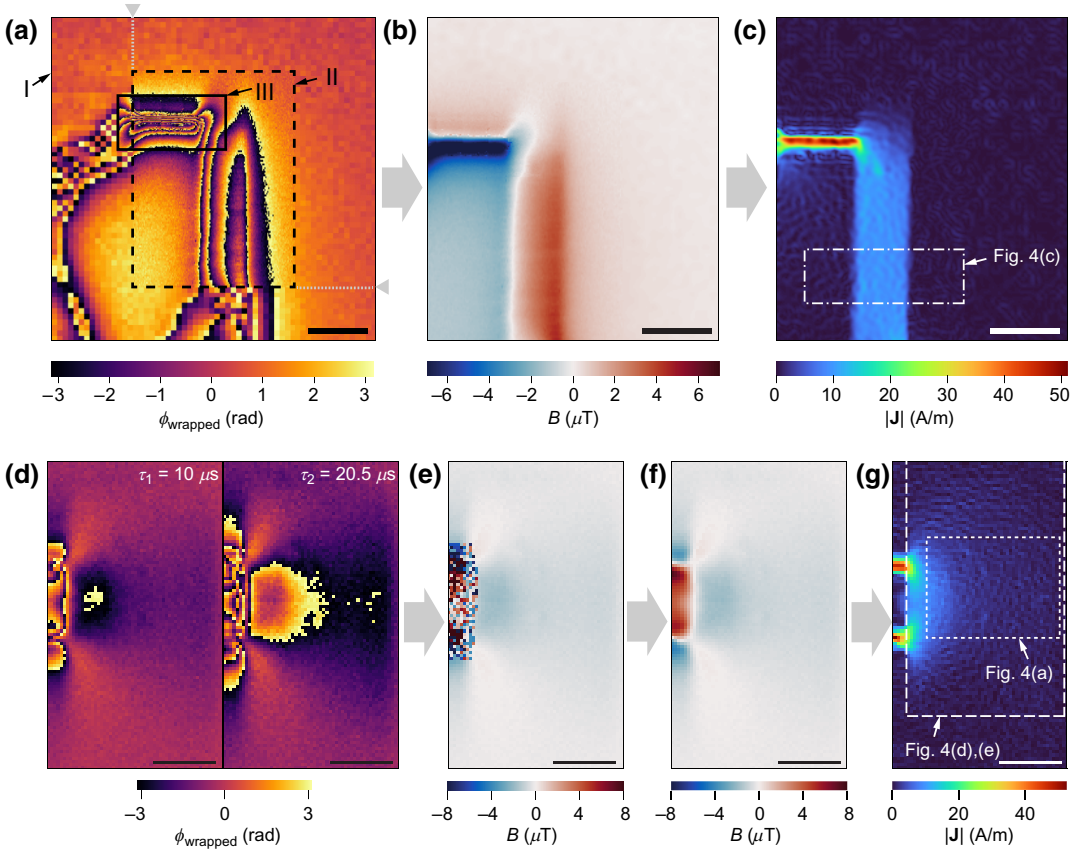

FIG. 3. Phase-unwrapping and current-density reconstruction. (a)–(c) Variable grid size method, demonstrated on device B with $I_{SD} \approx 7.2$ μA between contacts 1 and 2. (a) Map of the quantum phase composed of three scans (I–III) with varying pixel sizes (I, 100 × 100 nm; II, 19 × 33 nm; III, 20 × 10 nm). Gray markers denote the subsection of the image processed in (b),(c). (b) Map of the magnetic field after applying a phase unwrapping algorithm. B represents the vector field component along the N-V center's anisotropy axis [28]. (c) Map of the current density reconstructed from (b). (d)–(g) Bayesian inference method, demonstrated on device A with $I_{SD} \approx 10$ μA between contacts 1 and 3. (d) Maps of the quantum phase recorded with $\tau_1 = 10$ μs and $\tau_2 = 20.5$ μs. (e) Map of the magnetic field after the first phase-unwrapping step. (f) Map of the magnetic field after the second phase-unwrapping step that corrects for spatial smoothness. (g) Map of the current density. Dashed white boxes in (c),(g) refer to Fig. 4. Filter cutoff in (c),(g) is $\lambda = z$, where z is the standoff distance. Scale bars are 1 μm.

envelope to $P(B)$ that narrows down the set of possible probability maxima. We then update $P(B)$ for all pixels by traversing the grid multiple times until convergence is achieved. The results of this iterative phase estimation algorithm are presented in Figs. 3(f) and 3(g). For the reconstructed field image, we find an increase of the dynamic range by 6.7× compared to the right plot in Fig. 3(d). Overall, we find that both phase-unwrapping methods are successful in recovering the field maps; however, the variable-grid method is somewhat unsatisfactory due to image stitching and the possibility of image artifacts.

VI. TRANSPORT PHYSICS

We now turn our attention to the interpretation of the current density maps. In particular, we inspect them for possible spatial signatures of nonuniform conductivity [44–46] and hydrodynamic transport [9,11,12,27,47,48].

Figure 4(a) shows a section of device A on a magnified scale. While the current density is spatially smooth overall, we do observe channels of locally enhanced current flow (white arrows). Although these anomalies are of the order of a few microamperes per micrometer only, they are statistically significant and reproducible [28]. Comparison with the atomic force microscope (AFM) image [Fig. 4(b)] reveals that the anomalies are correlated with slight rises in the topography (black arrows). Similar statistically significant current density features are seen on device B [Fig. 4(c)]. While we do not know the microscopic origin of the current density variations, it is likely that they reflect variations in conductivity due to a varying background potential [49,50]. Although encapsulating graphene in h-BN helps reduce the effect of charge impurities from the substrate [51,52], the stacking process can lead to the formation of bubbles that act as dopants and local scatterers for transport [53]. This explanation

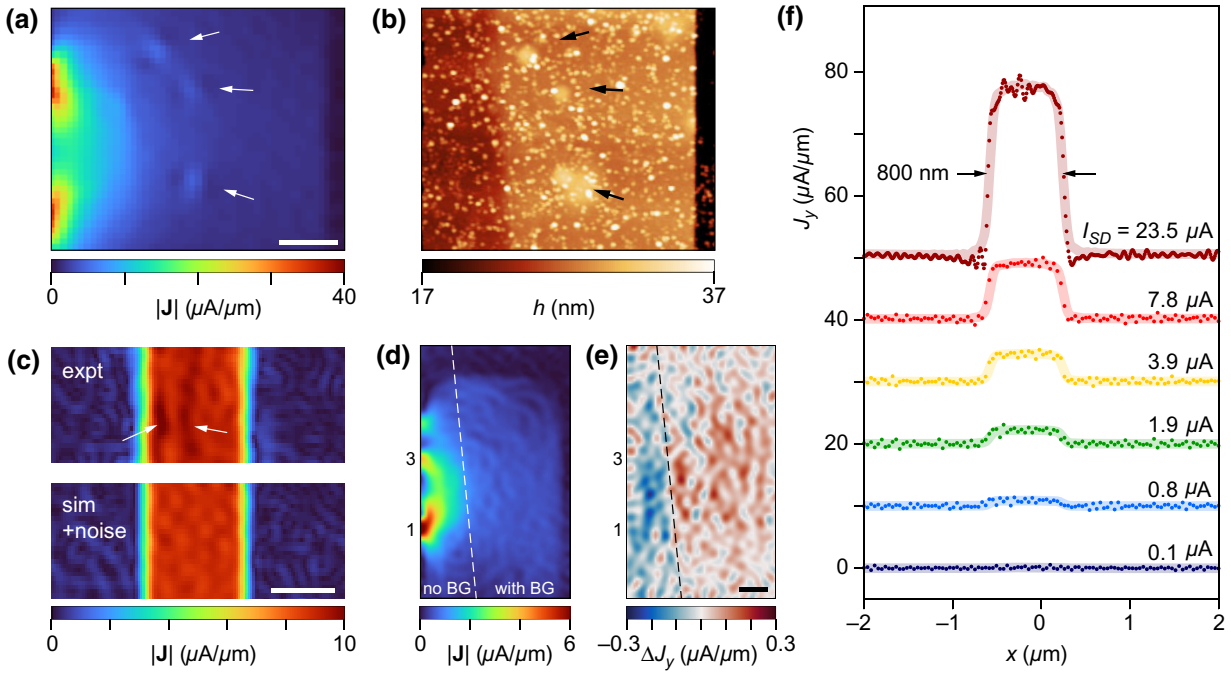

FIG. 4. Transport physics. (a) Magnified current density map of device A [dotted area in Fig. 3(g)]. Arrows indicate anomalies in the current flow. (b) Corresponding AFM topography. (c) Current density map of device B [dash-dotted area in Fig. 3(c)]. Upper map shows the experimental data. Lower map shows simulated data assuming a perfect rectangular conductor after adding the equivalent amount of white noise. Arrows indicate channels of increased current flow in the experiment. (d) Current density map of device A [dashed area in Fig. 3(g)] for $V_{\mathrm{BG}} = 0$ V. Note that the back gate only covers the right part of the device, indicated by a dashed line. (e) Differential current density map ΔJ_y obtained by subtracting $J_y^{(V_{\mathrm{BG}}=-2\ \mathrm{V})} - J_y^{(V_{\mathrm{BG}}=0\ \mathrm{V})}$. (f) Reconstructed current density profiles J_y across the Hall-bar channel (device B). Dots are the data and solid line is a calculation for a uniform current density profile. I_{SD} is the applied source-drain current. Step size is 10 nm for the $I_{SD} = 23.5$ μA curve and 40 nm for all other curves. Curves are vertically offset for clarity. Scale bars are 500 nm.

would be consistent with the correlated AFM topography observed with Figs. 4(a) and 4(b).

To further investigate the influence of the local potential, we record current density maps for different values of the back-gate voltage akin to Ref. [46]. Since the expected current density variations are small, we use a differential acquisition technique where two images are recorded synchronously by toggling V_{BG} between subsequent measurement cycles [Fig. 1(d)]. The synchronous imaging guarantees that neither spatial drifts nor temporal changes in the transport properties result in spurious signals in the differential image. Figure 4(d) shows a current density map for $V_{\mathrm{BG}} = 0$ V and Fig. 4(e) the difference image between a $V_{\mathrm{BG}} = -2$ V and $V_{\mathrm{BG}} = 0$ V map, respectively (see [28] for the full data set). These maps are recorded on device A where the graphite back gate only covers part of the device (separated by the dashed line). Consistent with a higher carrier density in the back-gated region (Fig. S1 in the Supplemental Material), the difference image is positive in the right portion of the map, confirming that current flow shifts to the high-conductivity region. Overall, Fig. 4(e) demonstrates that we can reliably detect small (approximately 5%–10%) changes in the flow pattern despite the presence of a large background current density. We further observe small leakage currents through the unconnected contacts 2 and 4 due to the relatively high modulation frequency of the source-drain current [28].

To reveal the possible presence of hydrodynamic transport effects, we analyze the current profile across the Hall-bar channel (device B). A hallmark (but not unique [9]) signature for hydrodynamic transport is a parabolic flow profile, rather than the uniform (rectangular) profile associated with diffusive transport [48,54]. Recent experiments on MLG have reported parabolic flow in channels of similar width at room temperature [12]. Figure 4(f) shows a set of line scans across the Hall-bar channel for applied currents 0.1–23.5 μA. All scans are taken near the charge neutrality point ($V_{\mathrm{BG}} = 0$ V) where the carrier-carrier scattering is predicted to be strongest [55]. We find that all scans exhibit a rectangular current density profile [background lines in Fig. 4(f)] consistent with transport that is fully in the diffusive regime. The absence of any hydrodynamic component could be due to a much lower carrier viscosity in BLG compared to MLG near charge

neutrality for BLG [27]. Even higher mobilities or cryogenic temperatures may be needed to observe the effect, if at all present.

VII. HIGH-SENSITIVITY SCANS

Finally, we explore the limits of our technique towards detection of small currents. In Figs. 5(a) and 5(b), we perform two-dimensional imaging on device A with a source-drain current of $I = 0.3\ \mu$A. To maximize sensitivity, we increase the ac current modulation to $f = 1.33$ MHz and use a dynamical decoupling sequence with $N = 128$ pulses to extend the interaction time to $\tau = 48\ \mu$s (Fig. S10 in the Supplemental Material) [56,57]. From separate high-resolution line scans, shown in Fig. 5(c), we extract an absolute magnetic field sensitivity of 4.6 nT for an averaging time of 120 s per pixel (see Fig. S3 in the Supplemental Material for full data). This corresponds to a per-root-Hertz sensitivity of 51 nT/$\sqrt{\text{Hz}}$, in good agreement with the nominal sensitivity expected for this N-V center tip (47 nT/$\sqrt{\text{Hz}}$; see [28]). Likewise, from Fig. 5(d), we find an absolute current sensitivity of 20 nA/μm corresponding to a per-root-Hz sensitivity of approximately 0.2 μA/(μm$\sqrt{\text{Hz}}$).

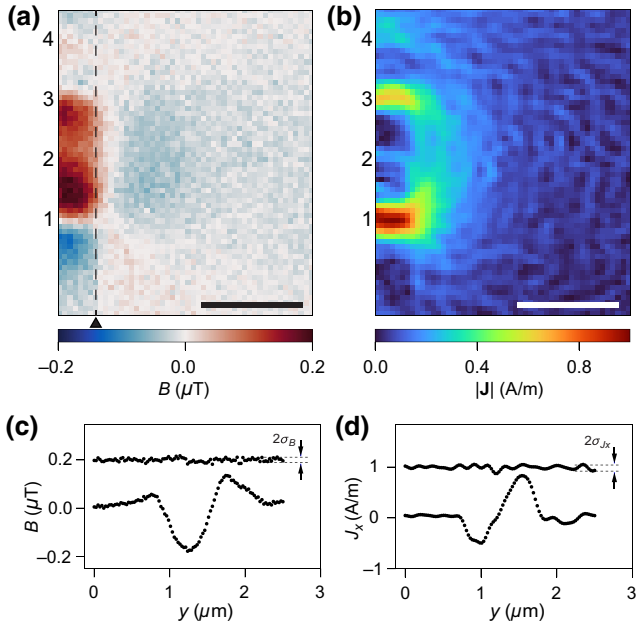

FIG. 5. Imaging of a 0.3 μA current. (a),(b) High-sensitivity magnetic field and current density maps recorded on device A. A current of $I_{SD} = 0.3\ \mu$A and $f = 1.33$ MHz is injected into terminal 1 and collected at terminal 3. Some current leakage through the floating terminals 2 and 4 is also observed. Data are recorded using a dynamical decoupling sequence with $N = 128$ refocusing pulses and $\tau = 48\ \mu$s. Scale bars are 1 μm and filter cutoff in (b) is $\lambda = 1.5z$. (c) Best-effort magnetic line scan along the dashed line in (a). For this scan, current is injected into terminal 2 and collected at terminal 1, and measurement parameters are $N = 128$, $\tau = 38\ \mu$s, and $f = 1.68$ MHz. Each pixel represents a 120 s average. The upper trace (vertically offset for clarity) shows the difference between two line scans. The standard deviation extracted from the point-to-point difference is $\sigma_B = 4.6$ nT [28]. (d) Corresponding current density line scan with a standard deviation of $\sigma_{J_x} = 20$ nA/μm.

VIII. CONCLUSION

In summary, we report on sensitive imaging of current flow in two-dimensional conductors using scanning diamond magnetometry. We introduce a set of methods for increasing the sensitivity and dynamic range of the technique, for resolving small current density variations by synchronous differential imaging, and for mitigating undesired side-effects of magnetometry operation (due to, for example, the scanning tip, laser, and microwave pulses) on the electronic transport. These advances allow us to reveal subtle spatial variations in the current density in BLG devices, including anomalies resulting from bubbles in the h-BN encapsulation and tuning of the flow pattern via the back-gate potential. We also provide evidence that current flow is fully in the diffusive regime with no signs of carrier viscosity.

The sensitivity demonstrated in our work (approximately 50 nT/$\sqrt{\text{Hz}}$) compares well to those reached with superconducting quantum interference devices mounted on scanning tips (approximately 30 nT/$\sqrt{\text{Hz}}$, Ref. [7]). The latter have recently allowed for impressive advances in the imaging of, for example, topological edge currents [7] or twist-angle disorder [8], but are confined to cryogenic temperatures. Looking forward, our techniques will therefore be especially useful for studying transport features over a wide temperature range, include hydrodynamic "whirlpools" [58], the graphene Tesla valve [59], the onset of nonlinearity in transport phenomena [17], or the Stokes paradox in viscous two-dimensional fluids [60].

ACKNOWLEDGMENTS

We thank M. Eich, A. Popert, F. de Vries, H. Overweg, and A. Kurzmann for advice with the device fabrication, Z. Ding for support during preparatory experiments, and P. Märki and the FIRST-Lab clean-room staff for technical support. This work was supported by the European Research Council through ERC CoG 817720 (IMAGINE), Swiss National Science Foundation (SNSF) Project Grant No. 200020_175600, the National Centre of Competence in Research in Quantum Science and Technology (NCCR QSIT) Project Grant No. 51NF40-185902, and the (ASTERIQS) program, Grant No. 820394, of the European Commission. K.W. and T.T. acknowledge support from the Elemental Strategy Initiative conducted by the MEXT, Japan (Grant No. JPMXP0112101001) and JSPS KAKENHI (Grants No. 19H05790 and No. JP20H00354).

[1] E. Marchiori, L. Ceccarelli, N. Rossi, L. Lorenzelli, C. L. Degen, and M. Poggio, Nanoscale magnetic field imaging for 2D materials, Nat. Rev. Phys **4**, 49 (2022).

[2] M. A. Topinka, B. J. Leroy, R. M. Westervelt, S. E. J. Shaw, R. Fleischmann, E. J. Heller, K. D. Maranowski, and A. C. Gossard, Coherent branched flow in a two-dimensional electron gas, Nature **410**, 183 (2001).

[3] J. Berezovsky, M. F. Borunda, E. J. Heller, and R. M. Westervelt, Imaging coherent transport in graphene (part i): Mapping universal conductance fluctuations, Nanotechnology **21**, 274013 (2010).

[4] S. Bhandari, G. H. Lee, K. Watanabe, T. Taniguchi, P. Kim, and R. M. Westervelt, Imaging electron flow from collimating contacts in graphene, 2D Mater. **5**, 021003 (2018).

[5] B. A. Braem, F. M. D. Pellegrino, A. Principi, M. Röösli, C. Gold, S. Hennel, J. V. Koski, M. Berl, W. Dietsche, W. Wegscheider, M. Polini, T. Ihn, and K. Ensslin, Scanning gate microscopy in a viscous electron fluid, Phys. Rev. B **98**, 241304 (2018).

[6] D. Halbertal, J. Cuppens, M. B. Shalom, L. Embon, N. Shadmi, Y. Anahory, H. R. Naren, J. Sarkar, A. Uri, Y. Ronen, Y. Myasoedov, L. S. Levitov, E. Joselevich, A. K. Geim, and E. Zeldov, Nanoscale thermal imaging of dissipation in quantum systems, Nature **539**, 407 (2016).

[7] A. Uri, Y. Kim, K. Bagani, C. K. Lewandowski, S. Grover, N. Auerbach, E. O. Lachman, Y. Myasoedov, T. Taniguchi, K. Watanabe, J. Smet, and E. Zeldov, Nanoscale imaging of equilibrium quantum Hall edge currents and of the magnetic monopole response in graphene, Nat. Phys. **16**, 164 (2020).

[8] A. Uri, S. Grover, Y. Cao, J. Crosse, K. Bagani, D. Rodan-legrain, Y. Myasoedov, K. Watanabe, T. Taniguchi, P. Moon, M. Koshino, P. Jarillo-Herrero, and E. Zeldov, Mapping the twist-angle disorder and landau levels in magic-angle graphene, Nature **581**, 47 (2020).

[9] J. A. Sulpizio, L. Ella, A. Rozen, J. Birkbeck, D. J. Perello, D. Dutta, M. Ben-shalom, T. Taniguchi, K. Watanabe, T. Holder, R. Queiroz, A. Principi, A. Stern, T. Scaffidi, A. K. Geim, and S. Ilani, Visualizing Poiseuille flow of hydrodynamic electrons, Nature **576**, 75 (2019).

[10] L. Ella, A. Rozen, J. Birkbeck, M. Ben-shalom, D. Perello, J. Zultak, T. Taniguchi, K. Watanabe, A. K. Geim, S. Ilani, and J. A. Sulpizio, Simultaneous voltage and current density imaging of flowing electrons in two dimensions, Nat. Nanotechnol. **14**, 480 (2019).

[11] A. Jenkins, S. Baumann, H. Zhou, S. A. Meynell, D. Yang, K. Watanabe, T. Taniguchi, A. Lucas, A. F. Young, and A. C. B. Jayich, Imaging the breakdown of ohmic transport in graphene, (2020), ArXiv:2002.05065.

[12] M. J. H. Ku, T. X. Zhou, Q. Li, Y. J. Shin, J. K. Shi, C. Burch, L. E. Anderson, A. T. Pierce, Y. Xie, A. Hamo, U. Vool, H. Zhang, F. Casola, T. Taniguchi, K. Watanabe, M. M. Fogler, P. Kim, A. Yacoby, and R. L. Walsworth, Imaging viscous flow of the Dirac fluid in graphene, Nature **583**, 537 (2020).

[13] M. Lee, S. Jang, W. Jung, Y. Lee, T. Taniguchi, K. Watanabe, H. Kim, H. Park, G. Lee, and D. Lee, Mapping current profiles of point-contacted graphene devices using single-spin scanning magnetometer, Appl. Phys. Lett. **118**, 033101 (2021).

[14] U. Vool, A. Hamo, G. Varnavides, Y. Wang, T. X. Zhou, N. Kumar, Y. Dovzhenko, Z. Qiu, C. A. C. Garcia, A. T. Pierce, J. Gooth, P. Anikeeva, C. Felser, P. Narang, and A. Yacoby, Imaging phonon-mediated hydrodynamic flow in WTe_2, Nat. Phys. (2021).

[15] K. Chang, A. Eichler, J. Rhensius, L. Lorenzelli, and C. L. Degen, Nanoscale imaging of current density with a single-spin magnetometer, Nano. Lett. **17**, 2367 (2017).

[16] A. M. R. Baker, J. A. Alexander-Webber, T. Altebaeumer, and R. J. Nicholas, Energy relaxation for hot Dirac fermions in graphene and breakdown of the quantum Hall effect, Phys. Rev. B **85**, 115403 (2012).

[17] L. P. Kouwenhoven, B. J. van Wees, C. J. P. M. Harmans, J. G. Williamson, H. van Houten, C. W. J. Beenakker, C. T. Foxon, and J. J. Harris, Nonlinear conductance of quantum point contacts, Phys. Rev. B **39**, 8040 (1989).

[18] M. A. Eriksson, R. G. Beck, M. Topinka, J. A. Katine, R. M. Westervelt, K. L. Campman, and A. C. Gossard, Cryogenic scanning probe characterization of semiconductor nanostructures, Appl. Phys. Lett. **69**, 671 (1996).

[19] E. J. H. Lee, K. Balasubramanian, R. T. Weitz, M. Burghard, and K. Kern, Contact and edge effects in graphene devices, Nat. Nanotechnol. **3**, 486 (2008).

[20] H. Cao, G. Aivazian, Z. Fei, J. Ross, D. H. Cobden, and X. Xu, Photo-Nernst current in graphene, Nat. Phys. **12**, 236 (2016).

[21] L. Ju, J. Velasco, E. Huang, S. Kahn, C. Nosiglia, H.-Z. Tsai, W. Yang, T. Taniguchi, K. Watanabe, Y. Zhang, G. Zhang, M. Crommie, A. Zettl, and F. Wang, Photoinduced doping in heterostructures of graphene and boron nitride, Nat. Nanotechnol. **9**, 348 (2014).

[22] L. Rondin, J. P. Tetienne, T. Hingant, J. F. Roch, P. Maletinsky, and V. Jacques, Magnetometry with nitrogen-vacancy defects in diamond, Rep. Prog. Phys. **77**, 056503 (2014).

[23] C. L. Degen, Scanning magnetic field microscope with a diamond single-spin sensor, Appl. Phys. Lett. **92**, 243111 (2008).

[24] G. Balasubramanian, I. Y. Chan, R. Kolesov, M. Al-Hmoud, J. Tisler, C. Shin, C. Kim, A. Wojcik, P. R. Hemmer, A. Krueger, T. Hanke, A. Leitenstorfer, R. Bratschitsch, F. Jelezko, and J. Wrachtrup, Nanoscale imaging magnetometry with diamond spins under ambient conditions, Nature **455**, 648 (2008).

[25] L. Wang, I. Meric, P. Y. Huang, Q. Gao, Y. Gao, H. Tran, T. Taniguchi, K. Watanabe, L. M. Campos, D. A. Muller, J. Guo, P. Kim, J. Hone, K. L. Shepard, and C. R. Dean, One-dimensional electrical contact to a two-dimensional material, Science **342**, 614 (2013).

[26] P. J. Zomer, M. H. D. Guimarães, J. C. Brant, N. Tombros, and B. J. van Wees, Fast pick up technique for high quality heterostructures of bilayer graphene and hexagonal boron nitride, Appl. Phys. Lett. **105**, 013101 (2014).

[27] D. A. Bandurin, I. Torre, R. K. Kumar, M. B. Shalom, A. Tomadin, A. Principi, G. H. Auton, E. Khestanova, K. S. Novoselov, I. V. Grigorieva, L. A. Ponomarenko, A. K. Geim, and M. Polini, Negative local resistance caused by viscous electron backflow in graphene, Science **351**, 1055 (2016).

[28] See Supplemental Material at http://link.aps.org/supplemental/10.1103/PhysRevApplied.17.054008 for additional details on device fabrication and characterization, magnetic field sensitivities, phase unwrapping algorithms and spatial analysis of current density maps.
[29] T. Hingant, J.-P. Tetienne, L. Martínez, K. Garcia, D. Ravelosona, J.-F. Roch, and V. Jacques, Measuring the Magnetic Moment Density in Patterned Ultrathin Ferromagnets with Submicrometer Resolution, Phys. Rev. Appl. **4**, 014003 (2015).
[30] QZabre AG, https://qzabre.com.
[31] S. Kotler, N. Akerman, Y. Glickman, A. Keselman, and R. Ozeri, Single-ion quantum lock-in amplifier, Nature **473**, 61 (2011).
[32] G. D. Lange, D. Riste, V. V. Dobrovitski, and R. Hanson, Single-Spin Magnetometry with Multipulse Sensing Sequences, Phys. Rev. Lett. **106**, 080802 (2011).
[33] C. Degen, F. Reinhard, and P. Cappellaro, Quantum sensing, Rev. Mod. Phys. **89**, 035002 (2017).
[34] H. S. Knowles, D. M. Kara, and M. Atature, Demonstration of a Coherent Electronic Spin Cluster in Diamond, Phys. Rev. Lett. **117**, 100802 (2016).
[35] D. C. Ghiglia and M. D. Pritt, *Two-Dimensional Phase Unwrapping: Theory, Algorithms, and Software* (Wiley, New York, NY, 1998).
[36] J. Park, Y. H. Ahn, and C. Ruiz-Vargas, Imaging of photocurrent generation and collection in single-layer graphene, Nano Lett. **9**, 1742 (2009).
[37] We use the *phase_unwrap* method provided by the python package scikit-image, PeerJ **2**, e453 (2014).
[38] M. A. Herráez, D. R. Burton, M. J. Lalor, and M. A. Gdeisat, Fast two-dimensional phase-unwrapping algorithm based on sorting by reliability following a noncontinuous path, Appl. Opt. **41**, 7437 (2002).
[39] B. J. Roth, N. G. Sepulveda, and J. P. Wikswo, Using a magnetometer to image a two-dimensional current distribution, J. Appl. Phys. **65**, 361 (1989).
[40] D. Broadway, S. Lillie, S. Scholten, D. Rohner, N. Dontschuk, P. Maletinsky, J.-P. Tetienne, and L. Hollenberg, Improved Current Density and Magnetization Reconstruction through Vector Magnetic Field Measurements, Phys. Rev. Appl. **14**, 024076 (2020).
[41] L. Childress, M. V. G. Dutt, J. M. Taylor, A. S. Zibrov, F. Jelezko, J. Wrachtrup, P. R. Hemmer, and M. D. Lukin, Coherent dynamics of coupled electron and nuclear spin qubits in diamond, Science **314**, 281 (2006).
[42] N. M. Nusran, M. U. Momeen, and M. V. G. Dutt, High-dynamic-range magnetometry with a single electronic spin in diamond, Nat. Nanotechnol. **7**, 109 (2012).
[43] G. Waldherr, J. Beck, P. Neumann, R. S. Said, M. Nitsche, M. L. Markham, D. J. Twitchen, J. Twamley, F. Jelezko, and J. Wrachtrup, High-dynamic-range magnetometry with a single nuclear spin in diamond, Nat. Nanotechnol. **7**, 105 (2012).
[44] K. W. Clark, X.-G. Zhang, I. V. Vlassiouk, G. He, R. M. Feenstra, and A.-P. Li, Spatially resolved mapping of electrical conductivity across individual domain (Grain) boundaries in graphene, ACS Nano **7**, 7956 (2013).
[45] J. P. Tetienne, N. Dontschuk, D. A. Broadway, A. Stacey, D. A. Simpson, and L. C. L. Hollenberg, Quantum imaging of current flow in graphene, Sci. Adv. **3**, e1602429 (2017).
[46] S. E. Lillie, N. Dontschuk, D. A. Broadway, D. L. Creedon, L. C. Hollenberg, and J.-P. Tetienne, Imaging Graphene Field-Effect Transistors on Diamond Using Nitrogen-Vacancy Microscopy, Phys. Rev. Appl. **12**, 024018 (2019).
[47] L. Levitov and G. Falkovich, Electron viscosity current vortices and negative nonlocal resistance in graphene, Nat. Phys. **12**, 672 (2016).
[48] I. Torre, A. Tomadin, A. K. Geim, and M. Polini, Nonlocal transport and the hydrodynamic shear viscosity in graphene, Phys. Rev. B **92**, 165433 (2015).
[49] N. Pascher, D. Bischoff, T. Ihn, and K. Ensslin, Scanning gate microscopy on a graphene nanoribbon, Appl. Phys. Lett. **101**, 063101 (2012).
[50] A. G. F. Garcia, M. Koenig, D. Goldhaber-Gordon, and K. Todd, Scanning gate microscopy of localized states in wide graphene constrictions, Phys. Rev. B **87**, 085446 (2013).
[51] C. R. Dean, A. F. Young, I. Meric, C. Lee, L. Wang, S. Sorgenfrei, K. Watanabe, T. Taniguchi, P. Kim, K. L. Shepard, and J. Hone, Boron nitride substrates for high-quality graphene electronics, Nat. Nanotech. **5**, 722 (2010).
[52] J. Xue, J. Sanchez-Yamagishi, D. Bulmash, P. Jacquod, A. Deshpande, K. Watanabe, T. Taniguchi, P. Jarillo-Herrero, and B. J. LeRoy, Scanning tunnelling microscopy and spectroscopy of ultra-flat graphene on hexagonal boron nitride, Nat. Mater. **10**, 282 (2011).
[53] N. Leconte, H. Kim, H.-J. Kim, D. H. Ha, K. Watanabe, T. Taniguchi, J. Jung, and S. Jung, Graphene bubbles and their role in graphene quantum transport, Nanoscale **9**, 6041 (2017).
[54] E. I. Kiselev and J. Schmalian, Boundary conditions of viscous electron flow, Phys. Rev. B **99**, 035430 (2019).
[55] D. Y. H. Ho, I. Yudhistira, N. Chakraborty, and S. Adam, Theoretical determination of hydrodynamic window in monolayer and bilayer graphene from scattering rates, Phys. Rev. B **97**, 121404 (2018).
[56] T. Gullion, D. B. Baker, and M. S. Conradi, New, compensated carr-purcell sequences, J. Magn. Res. **89**, 479 (1990).
[57] Y. Romach, C. Muller, T. Unden, L. Rogers, T. Isoda, K. Itoh, M. Markham, A. Stacey, J. Meijer, S. Pezzagna, B. Naydenov, L. McGuinness, N. Bar-Gill, and F. Jelezko, Spectroscopy of Surface-Induced Noise Using Shallow Spins in Diamond, Phys. Rev. Lett. **114**, 017601 (2015).
[58] K. A. Guerrero-Becerra, F. M. D. Pellegrino, and M. Polini, Magnetic hallmarks of viscous electron flow in graphene, Phys. Rev. B **99**, 041407 (2019).
[59] J. Geurs, Y. Kim, K. Watanabe, T. Taniguchi, P. Moon, and J. H. Smet, Rectification by hydrodynamic flow in an encapsulated graphene Tesla valve, (2020), ArXiv:2008.04862.
[60] A. Lucas, Stokes paradox in electronic Fermi liquids, Phys. Rev. B **95**, 115425 (2017).